Extreme ultraviolet light from a tin plasma driven by a 2-µm-wavelength laser

L. BEHNKE,[1] R. SCHUPP,[1] Z. BOUZA,[1,2] M. BAYRAKTAR,[3] Z. MAZZOTTA,[1,2] R. MEIJER,[1,2] J. SHEIL,[1] S. WITTE,[1,2] W. UBACHS,[1,2] R. HOEKSTRA,[1,4] AND O. O. VERSOLATO[1,2,*]

[1]*Advanced Research Center for Nanolithography, Science Park 106, 1098 XG Amsterdam, The Netherlands*
[2]*Department of Physics and Astronomy, and LaserLaB, Vrije Universiteit, De Boelelaan 1081, 1081 HV Amsterdam, The Netherlands*
[3]*Industrial Focus Group XUV Optics, MESA+ Institute for Nanotechnology, University of Twente, Drienerlolaan 5, 7522 NB Enschede, The Netherlands*
[4]*Zernike Institute for Advanced Materials, University of Groningen, Nijenborgh 4, 9747 AG Groningen, The Netherlands*
[*]versolato@arcnl.nl

Abstract: An experimental study of laser-produced plasmas is performed by irradiating a planar tin target by laser pulses, of 4.8 ns duration, produced from a KTP-based 2-µm-wavelength master oscillator power amplifier. Comparative spectroscopic investigations are performed for plasmas driven by 1-µm- and 2-µm-wavelength pulsed lasers, over a wide range of laser intensities spanning $0.5 - 5 \times 10^{11}$ W/cm ^{2}. Similar extreme ultraviolet (EUV) spectra in the 5.5–25.5 nm wavelength range and underlying plasma ionicities are obtained when the intensity ratio is kept fixed at $I_{1\mu m}/I_{2\mu m} = 2.4(7)$. Crucially, the conversion efficiency (CE) of 2-µm-laser energy into radiation within a 2% bandwidth centered at 13.5 nm relevant for industrial applications is found to be a factor of two larger, at a 60 degree observation angle, than in the case of the denser 1-µm-laser-driven plasma. Our findings regarding the scaling of the optimum laser intensity for efficient EUV generation and CE with drive laser wavelength are extended to other laser wavelengths using available literature data.

1. Introduction

Extreme-ultraviolet (EUV) lithography has successfully entered high-volume manufacturing, enabling the continued miniaturization of semiconductor devices. The required EUV light is generated from mass-limited tin-microdroplet laser-produced plasma (LPP) [1–5]. Multiply charged tin plasma ions are the atomic sources of EUV radiation near 13.5 nm wavelength [5–12]. Currently, CO_2-gas lasers operating at $\lambda = 10.6\,\mu m$ wavelength are used to drive the EUV-emitting plasma at a high conversion efficiency (CE) of laser energy into 'in-band' radiation, i.e. in a 2% wavelength bandwidth centered at 13.5 nm emitted into the half-sphere back towards the laser that is relevant for state-of-the-art EUV lithography. Solid-state lasers, operating at near- or mid-infrared wavelengths, may however become a viable alternative in the future. Such laser systems would potentially provide a smaller footprint, a significantly higher efficiency in converting electrical power to laser light, and may be scaled to much higher pulse energies and output powers which will enable even more powerful EUV light sources. However, the shorter drive laser wavelength of, e.g., the well-known Nd:YAG laser (1064 nm) is associated with large optical depths of EUV emitting plasmas [1]. Large optical depths may strongly limit the efficiency of such Nd:YAG-driven sources as opacity effects broaden the EUV spectrum well beyond the 2% wavelength acceptance bandwidth, thus reducing the spectral purity (SP) of the EUV plasma source [13–20]. SP is defined here as the ratio of in-band EUV energy to the total energy emitted in the 5.5–25.5 nm range. Simulation efforts indicate that a global optimum of the

efficiency of converting drive laser light into useful EUV radiation lies in between the well-known 1- and 10-µm cases [21]. In this range, thulium lasers, operating at 1.9-µm wavelength, appear promising [22]. The simulation efforts have produced predictions of CEs ranging from 1.2 times the CE of 1-µm-driven plasmas up to the much higher CEs achieved by 10-µm-driven plasmas (see below), depending on precise plasma conditions, when using such thulium lasers [21,23]. However, no experimental studies of plasmas driven by lasers in the 1- and 10-µm range, under conditions relevant for EUV emission, are yet available.

The current search for an optimum laser wavelength between 1 and 10 µm for driving EUV emitting plasma can be put in a broader context. Nishihara et al. [24] produced an overview of the key physics issues for optimizing EUV sources also with respect to drive laser wavelength. They furthermore provided simulation results using a power balance model for optimal drive laser intensities with predictions for obtainable CE, shown in Fig. 1, for an ideal case of plasma of single optimal density and temperature. In Fig. 1, the obtainable CE is shown to rise with drive laser wavelength from ~1% for the shortest wavelength, to ~6% for the longest one. The optimum laser intensity decreases with increasing laser wavelength. Several other groups performed simulations to establish optimal conditions for EUV production from plasma. For example, White et al. [20] computationally studied the impact of laser wavelength and power density in a comparison of Nd:YAG (at its fundamental wavelength and its third harmonic) and CO_2 lasers. Their results strongly favor the latter drive laser for reaching the highest CE values. Achieving optimum plasma conditions for efficient in-band EUV emission at sufficient brightness under non-idealized conditions involves trade-offs, maintaining sufficiently high optical depth for in-band transitions and limiting optical depth for weaker out-of-band transitions [25,26].

The conclusions from Nihishara et al. [24] are by and large supported by experiment. In the following, we present a brief literature review of experimentally obtained CE values and optimum laser intensities. The values reported are for planar solid pure-tin targets unless specified otherwise. The findings are summarized in Fig. 1. Starting at the shortest drive laser wavelength, Shevelko et al. [27] recorded a peak CE into a 1% bandwidth at 13.5 nm of 0.31% with a KrF laser pulse at 248 nm wavelength at a power density of 1×10^{12} W/cm^2. Kauffman et al. [28] achieved a CE of ~1% (as reported by Hayden et al. [19]) using frequency-doubled Nd:YAG pulses at 532 nm. They observed that the CE was highly sensitive to the incident laser pulse intensity, to peak at 2×10^{11} W/cm^2. Hayden et al. [19] demonstrated 2.2% CE using a pulsed Nd:YAG laser operating at its fundamental 1064 nm wavelength and an intensity of 2×10^{11} W/cm^2. Their findings are in line with those of Harilal et al. [29] who found a 2% CE value at 4×10^{11} W/cm^2 using the same drive wavelength. Tao et al. [30] studied the influence of focal spot size on in-band emission from Nd:YAG laser-produced Sn plasmas finding almost constant in-band conversion efficiency (at a ~2% value, consistent with Coons et al. [31]) of focal spot sizes of 60 to 500 µm thereby contrasting the findings of Spitzer et al. [32] (also see Sec. 3. below). In this work we find (see Sec. 3.) optimal SP and CE values at a Nd:YAG laser intensity of 3×10^{11} W/cm^2. Other studies (see Campos et al. [33] and references therein) showed that the optimum laser pulse parameters for obtaining the highest CE for CO_2 and Nd:YAG laser pulses are 6×10^{9} W/cm^2 and 6×10^{10} W/cm^2, respectively. A much larger ~5% CE value was reported by George et al. [34] at an intensity close to 1×10^{11} W/cm^2. For droplet pure-tin targets, CEs can be found with values ranging from 1.4% as reported by Giovannini et al. [35] to ~3% reported in Schupp et al. [14] both at a Nd:YAG laser intensity of 2×10^{11} W/cm^2 but using different plasma recipes. A similar 3% CE was obtained by Shimada et al. [36] from spherical solid tin targets that were illuminated uniformly with twelve beams from the 1.05µm-wavelength Gekko XII laser system.

Moving towards longer wavelengths, Tanaka et al. [18] estimated the maximum conversion efficiency for both CO_2 and Nd:YAG laser driven plasma to be 2% alike. Their work indicated an optimum drive laser intensity of 10^{10} W/cm^2 for the CO_2 driver and several 10^{10} W/cm^2 for the Nd:YAG driver. Using a CO_2 driver, Harilal et al. [37] found CEs approaching 4%
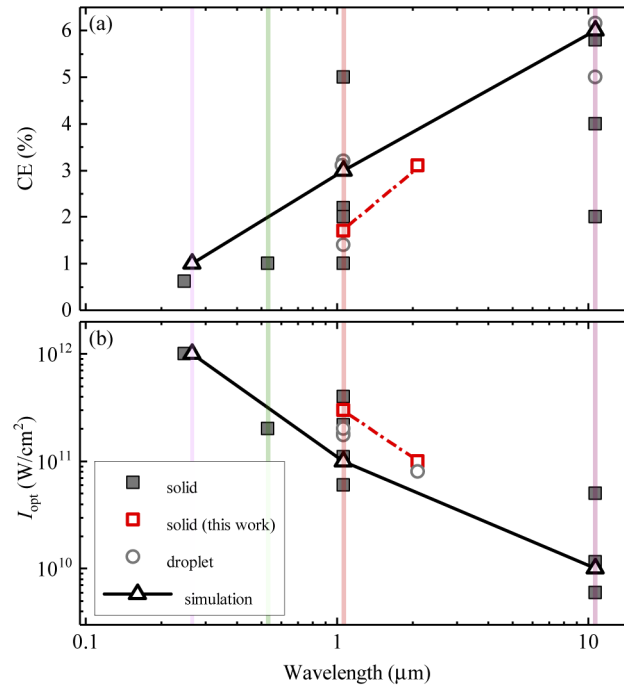
Fig. 1. (a) Conversion efficiency (CE) and (b) optimum laser intensity (I_{opt}) values as a function of drive laser wavelength, as obtained from previous experiments on planar solid (full gray squares) and droplet (open gray circles) tin targets (data from Refs. [14–16,18,19,27–31,33,34,36–43], see main text). Overlapping data points are shifted vertically for visibility. Simulation results [24] for plasma under optimal conditions are shown (open black triangles) connected by straight lines. The vertical lines, from right to left, indicate the wavelength of the CO_2 laser and that of the Nd:YAG laser and its second and fourth harmonics. The results of the current work are shown as open red squares. See main text for further details.

when optimizing the focal spot size at a constant 6×10^9 W/cm^2 intensity (also see their more recent work [16]). Ueno et al. [38] found a similar value of 4% using a cavity target. More recently, a maximum CE of 5.8% was found by Amano et al. [39] using a CO_2 laser intensity of 5×10^{10} W/cm^2 and a relatively short 5 ns pulse duration. Using a CO_2 driver and droplet pure-tin targets, CE values of ~5% were reported by the company Gigaphoton by Mizoguchi et al. [40] and ~6% by ASML company as presented by Fomenkov et al. [41]. These high CE values were obtained using multiple laser pulses that shape the liquid droplet target for optimal interaction with the CO_2 main pulse beam. Conclusions could also be drawn from obtained relative CE values where no absolute information is available. For example, Yamaura et al. [42] characterized EUV emission for 266 and 1064 nm drive laser wavelengths finding that the EUV emission exhibits a laser-wavelength dependence in terms of angular distribution. Pronounced absorption dips appear in the EUV emission spectra in the case of the short-wavelength driver, indicating a reduced spectral purity which may lead to a lower obtainable CE. Freeman et al. [15] (also see the related work of Campos et al. [33]) showed highest in-band emission and spectral purity from the longest wavelength drive laser when comparing 1064, 532, and 266 nm wavelength experiments.

In this work we present a study of the EUV emission spectrum of a 2-μm-wavelength-LPP generated from a planar tin target, entering the territory of wavelengths in between 1 and 10 μm.

We find highest SP and CE at 1×10^{11} W/cm^2. In a complementary study [43] our team finds that a similar intensity of 8×10^{10} W/cm^2 optimizes SP for pure-tin droplet targets using 2 µm wavelength drive laser light. Those droplet-target experiments however produced insignificant CE due to the poor geometrical overlap of laser pulse and target. This drawback is absent in the current work where complete laser-target overlap is guaranteed and relevant CE values can be obtained. Our current studies are not intended to maximize CE but rather to provide a meaningful comparison of 1- to 2-µm drive laser cases. The 2-µm laser light in this work is obtained from a master oscillator power amplifier (MOPA) based on a series of KTP crystals pumped by a Nd:YAG laser. This setup enables assessing the potential of thulium lasers without the expense of developing and building one. The obtained EUV spectra and CEs are compared to those obtained from Nd:YAG-LPP under otherwise very similar conditions.

2. Experimental setup

In this work we present an experimental study of an LPP generated by illuminating a planar solid tin target of 99.995 % purity with pulsed lasers having wavelengths of 1 µm and 2 µm. The target is mounted on a two-axis translation stage inside a vacuum chamber pumped to 1×10^{-6} mbar. The target is moved after two laser shots per position to prevent crater formation influencing the EUV emission. Spectral emission in the 5–25 nm range is recorded by means of a transmission grating spectrometer positioned at 60 degrees with respect to the incoming laser (see Fig. 2). The spectrometer is operated with a slit width of 25 µm and a 10 000 lines/mm grating. The dispersed light is collected on a back-illuminated charge-coupled device. The dispersive axis is calibrated using reference spectra comprising well-known Al^{3+} and Al^{4+} line features between 11 and 16 nm wavelength [44]. The spectra are corrected for second-order contributions above 11 nm wavelength by utilizing the tabulated second-order diffraction efficiency [45]. More details on the spectrometer and post-processing of the images are provided in Refs. [45] and [14]. To obtain the absolute amount of EUV radiation emitted in a 2 % bandwidth around 13.5 nm, a calibrated EUV photodiode assembly [14] is used. It is installed at an angle of −60°, mirroring the alignment of the spectrometer cf. Fig. 2(a). This photodiode assembly consists of a Mo/Si multilayer mirror that reflects the in-band radiation onto a photodiode. The photodiode is coated with a Si/Zr coating in order to block infrared light.

 The 2-µm light source comprises a KTP-based MOPA operated in type-2 phase matching following the approach of Arisholm et al. [46]. The MOPA setup is pumped at a 10 Hz repetition rate by a seeded Q-switched Nd:YAG laser (QuantaRay 250-10 PRO) providing pulses of 10 ns duration (at full width at half maximum, FWHM). First, a 2170 nm idler seed beam of 1.8 mJ energy is created in a singly-resonant optical parametric oscillator (OPO). To create this seed beam, 18 mJ pump light is demagnified to a beam diameter of 1.5 mm and is coupled into the OPO which is operated in a collinear alignment. About 20 % of the pump radiation is converted into a 2090 nm wavelength signal beam and a 2170 nm idler beam. At the exit of the OPO a dichroic mirror separates the signal and idler beams from the remaining pump radiation. The idler beam is subsequently expanded to 11 mm in diameter to seed the OPA, while the signal beam is removed through polarization optics. The OPO and OPA are pumped by the same laser. To achieve highest efficiency in the OPA, 1.3 J of the pump laser light is delayed by 1.3 ns and is reduced to a beam size of 10 mm in diameter. Seed and pump beams are overlapped on a dichroic mirror after which they pass three 18-mm-long KTP crystals. The crystal orientation is alternated to compensate for walk-off. A total energy of 260 mJ is achieved in signal and idler combined. Pump and signal beams are separated from the idler using a dichroic mirror and polarization optics, respectively. To adjust the idler beam energy a combination of a half-wave plate and a polarizer is installed before the focusing optics. The size of the focal spot on the target is 72×128 µm (FWHM). The asymmetry in the focal spot size is caused by the slightly higher beam quality on the horizontal, *x*-axis of the beam (cf. Fig. 2(b)). The pulse duration is
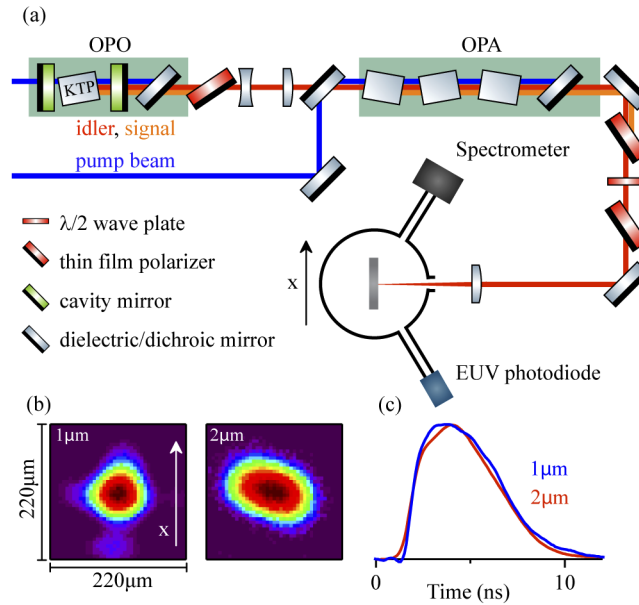
Fig. 2. (a) Schematic representation of the experimental setup. A master oscillator power amplifier (MOPA) setup, comprising an optical parametric oscillator (OPO) and an optical parametric amplifier (OPA), is pumped by a Nd:YAG laser. The 2-μm idler beam from the MOPA is focused onto a planar tin target to create plasma. The EUV emission from the plasma is captured by a transmission grating spectrometer and a calibrated EUV photodiode. (b) Spatial profiles with Gaussian spot sizes of 66×66 μm FWHM for the 1-μm drive laser and 72×128 μm FWHM for the 2-μm drive laser. (c) Temporal profiles of the 1- and 2-μm drive lasers.

4.8 ns (FWHM); uncertainties in determining the pulse duration are at or below 0.5 ns. The pulse has a short rise time of ~1 ns; its fall time is significantly longer and is seen to follow the pulse shape of the seed beam.

A seeded, in-house built Nd:YAG laser is used as the 1-μm laser light source to drive plasma [47]. The laser employs two electro-optical modulators to create temporal profiles of the desired shape. Here the temporal profile was shaped to match that of the idler of the MOPA (cf. Fig. 2(c)). A lens is used to focus the laser beam onto the tin target to a symmetric spot size of 66 μm (FWHM) closely matching the horizontal beam spot size of the idler beam in the measurement plane (cf. Fig. 2(b)).

3.   Results

In the following, we assess the potential of a 2-μm-wavelength tin-plasma driver by studying the spectral characteristics with emphasis on EUV in-band radiation. Fig. 3(a) shows EUV spectra obtained when the beam intensity $I_{2\mu m}$ is varied in a $0.2 - 1.9 \times 10^{11}$ W/cm^2 range. The intensity of 2-μm driver $I_{2\mu m}$ is given by the peak intensity in time and space by $I_{2\mu m} = (2\sqrt{2\ln 2/2\pi})^3 E_{2\mu m}/abt_p$. Here, $E_{2\mu m}$ is the laser energy, a and b are the Gaussian FWHM sizes along the major and minor axis of the elliptical beam, and t_p is the FWHM pulse duration. Spectral features belonging to Sn^{5+} to Sn^{15+} are observed in the studied spectral range [6,8,11,48–50]. At the lower laser intensities, spectral features belonging to Sn^{5+} to Sn^{8+} are visible. At higher laser intensities, spectral features related to the higher charge states Sn^{10+} to Sn^{15+} are prominent. Spectral emission from these charge states also becomes visible in the short-wavelength region

of the spectra below 12 nm. The evolution of spectral features in this wavelength regime gives direct qualitative insight into the underlying charge state distribution as the contributions from the individual charge states can be identified [49].
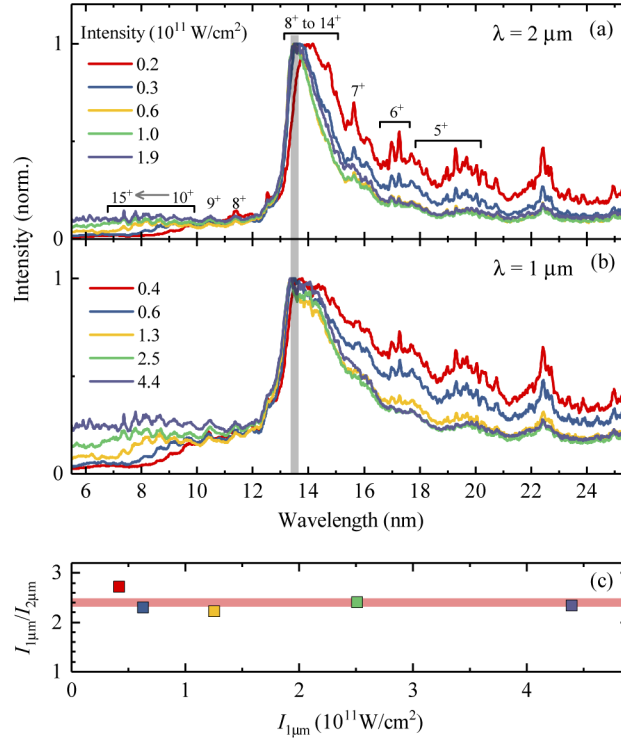
Fig. 3. Spectra from plasma produced from a planar solid tin target irradiated with laser pulses at various intensities of the (a) 2-μm driver (4.8 ns pulse duration, Gaussian spot size of 72×128 μm). The emission features attributed to the various Sn ions are labeled by the respective charge state. (b) Spectra from tin plasma driven by a 1-μm-beam (4.4 ns pulse duration, Gaussian spot size of 66×66 μm). The gray vertical band indicates a 2% bandwidth centered at 13.5 nm. (c) Ratio of intensities of 1- and 2-μm drive laser beams needed to obtain spectra with matching short-wavelength features. The red line indicates the average ratio.

For comparison, in Fig. 3(b) a set of spectra is presented that was obtained using the 1-μm-wavelength driver. Emission spectra are obtained for beam intensities $I_{1\mu m}$ ranging $0.4 - 4.4 \times 10^{11}$ W/cm^2. $I_{1\mu m}$ is defined analogously to $I_{2\mu m}$. The beam intensities are selected such that similar short-wavelength features are obtained as in the respective 2-μm cases. The laser intensity at which any particular charge state distribution is obtained, is lower for the 2-μm case by about a factor two. The evolution of spectral features with laser intensity appears to be similar, comparing Fig. 3(a) and (b).

To study this difference in more detail, pairs of intensities $I_{1\mu m}$ and $I_{2\mu m}$ were chosen such that the short-wavelength spectral features, ranging from 6 to 10 nm, in the respective emission spectra are best matching. In Fig. 3(c), the ratio of thus selected pairs $I_{1\mu m}/I_{2\mu m}$ is plotted versus $I_{1\mu m}$. On average the 1-μm driver requires a constant factor 2.4(7) higher intensity to reach the same effective charge state distribution of the plasma when compared to the 2-μm case. The number in brackets in the ratio 2.4(7) indicates the overall uncertainty which is dominated by systematic uncertainty. This ratio is very similar to the one found, at a value of 2.1(6), for droplet-target
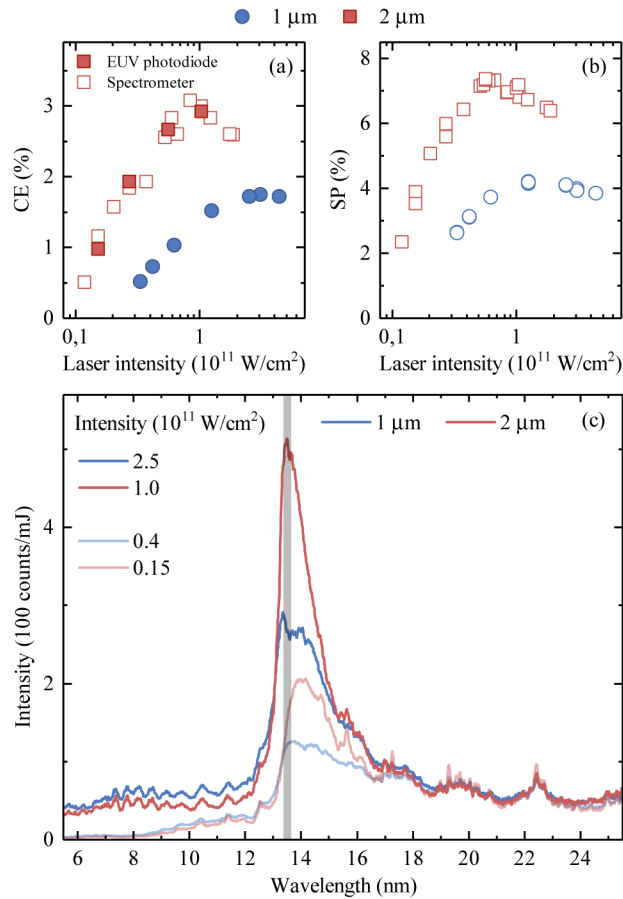
Fig. 4. Comparison of tin plasma emission characteristics for the 1- and 2-μm drivers: (a) Dependency of conversion efficiency (CE) on drive laser intensity for both drivers. The plot shows CE directly captured by a calibrated EUV photodiode, mounted under a 60 degree angle (cf. Fig. 2), as well as CE obtained from the absolute in-band measurements of the spectra, all assuming isotropic emission. (b) Spectral purity (SP) versus the intensity of the corresponding drive laser. (c) Juxtaposition of emission spectra. The intensity counts of the spectrometer are divided by the drive laser energy.

experiments using the same drive laser [43]. From the simulation work of Nishihara et al. [24] presented also in Sec. 1. it is clear that the relation between the optimum laser intensity and the laser wavelength can be approximated from the product $I\lambda^{1.2}$ (rather than $I\lambda^2$) because the ion density n_i where the in-band emission mostly occurs is much lower than the critical density $n_c \propto \lambda^{-2}$ for the relatively short-wavelength lasers. Studies on quasi-stationary ablation fronts [51] relevant for our current investigations support the findings of Nishihara et al. related to the scaling relations by pointing out that significant laser absorption occurs in the underdense coronal region, before the critical density surface. The theoretical scaling relations are fully in line with our current findings and with previous experiments as presented in our review in Sec. 1. and shed light on the physics origins of the plasma-emission of EUV light. Further radiation-hydrodynamic simulations (as presented in Ref. [43] and [52] for the droplet-target case) are however required for the current planar target case to investigate the details of the evolution of the relevant plasma conditions and their dependence on drive laser wavelength.

In Fig. 4(a), CE is plotted versus drive laser intensity for the 1-μm and 2-μm cases. The measured in-band radiation is extrapolated from the measurement at 60° to the 2π steradian half-sphere facing the laser origin, assuming isotropic emission over this half-sphere. The open markers indicate data obtained from the spectra taken with the spectrometer under the same angle of 60°. Here, the measured spectral intensities integrated over the in-band range are calibrated by comparison to the in-band energies measured by the EUV photodiode. These in-band energies are measured simultaneously with the spectra. From literature, it is evident that the EUV emission from LPPs from planar solid targets is slightly anisotropic [53]. Several studies have indicated that the angular dependence of EUV emission is nearly independent on the focal spot size and the pulse duration [53–55]. Hence, remaining differences in laser beam characteristics, which were carefully matched in our experiments, are not expected to have a significant impact on our observations. Changing the drive wavelength for a tin-LPP on a planar solid target from 266 nm to 1 μm was found to lead to a reduced angular dependence of the in-band emission [42]. For droplet targets, a 10-μm-driven LPP was shown to exhibit only a slightly reduced anisotropy of the in-band emission in comparison to the 1-μm-driven LPP [56] and thus the relatively small step to 2-μm laser radiation is not expected to change the current EUV emission anisotropy significantly. We furthermore note that the observation under the current, relatively large angle of 60° constitutes a representative measure of the overall CE [14,53–55]. Conclusions regarding final obtainable CE can be drawn only if also further laser parameters are varied and optimized. The laser focus size in particular is a sensitive parameter in the optimization. Spitzer et al. [32] presented a comprehensive database for source optimization by systematically varying parameters such as wavelength, pulse length, intensity, and spot size. The latter parameter was shown to have a significant influence on the obtainable conversion efficiency, a feature that was attributed to a changing dimensionality of the plasma expansion. Lateral heat conduction losses and multidimensional expansion losses reduce CE in the case of a small spot size [24]. Tao et al. [30] studied the influence of the focal spot size on in-band emission from Nd:YAG laser-produced Sn plasmas finding almost constant in-band conversion efficiency (at ~2% value) with focal spot sizes ranging 60 to 500 μm contrasting the findings of Spitzer et al. [32]. Harilal et al. [29] and Koay et al. [57] also demonstrated high CE using Sn targets with small focal spot sizes of 60 and 35 μm, respectively, albeit for tin-doped spherical targets in the latter case. The findings are further corroborated by Yuseph et al. [58] who found that a shorter length scale plasma reabsorbs less EUV light, resulting in a higher conversion efficiency for the smaller focal spot when comparing 26 and 150 μm spot size cases. In the current experiments the spot sizes and the temporal pulse shapes of the two drive wavelength cases (cf. Fig. 2) have been carefully tuned to be as close as possible, such that a relative comparison is apt.

The CE of the 2-μm-LPP rises with beam intensity, up to a maximum value of 3.1% at a laser intensity of 1.0×10^{11} W/cm^2. When further increasing the laser intensity CE decreases. For the 1-μm case, a similar rise of CE with increasing beam intensity is observed, with a maximum CE reaching 1.7%, i.e. only about half of that of the 2-μm case. The maximum CE for the 1-μm-LPP is reached at a laser intensity of 3.0×10^{11} W/cm^2. No decrease in CE is observed when moving to higher laser intensities, within the probed parameter space. Comparing the two drive laser cases, the relative difference in maximum CE amounts to a factor 1.8. The 1-μm-LPP requires significantly higher intensities to reach optimum CE. This is in line with the findings presented in Fig. 3(c).

Fig. 4(b) shows the spectral purity of both the 1-μm and the 2-μm-LPPs as a function of laser intensities. Both SP data sets show a behavior that is similar to that of the corresponding CE curves. Note again that SP is here defined as the ratio of in-band EUV energy to the total energy emitted in the 5.5–25.5 nm range. The maximum SP of the 2-μm-LPP is at 7.4% a factor 1.8 larger than the value of the 1-μm-LPP with a maximum of 4.2%. This maximum SP is reached at a laser intensity of 1×10^{11} W/cm^2, very close to the value of 0.8×10^{11} W/cm^2 found for

droplet-target experiments using the same drive laser [43]. The ratio of the maximum SPs is identical to the ratio of the maximum CEs. This indicates that the difference in conversion efficiency can be attributed to the decreased SP of the 1-μm-LPP. Figure 4(c) shows two pairs of matching emission spectra, i.e. plasmas having similar ionicities. The 2-μm-LPP spectra with the highest and lowest obtained CEs are shown. All spectra have been divided by the drive laser energy. The out-of-band features are seen to match well. It is apparent that a significant amount of spectral emission between 13 and 15 nm is missing in the 1-μm case compared to the 2-μm-LPP. This lack of emission in the unresolved transition array at 13.5 nm explains the reduced CE of the 1-μm-LPP.

To qualitatively explain the significant differences observed between the two drive laser cases, it is instructive to employ an intuitive two-zone radiation transport model. In this simple model, the emission from a hot plasma core zone ("zone 1") traverses a plasma zone ("zone 2") at a modestly lower density and temperature. Such a two-zone plasma approximates our experimental conditions where a laser beam with a Gaussian spatial intensity profile inhomogeneously heats the plasma. Further inhomogeneities are present along the laser beam propagation z-axis (see e.g. Ref. [51]). Our one-dimensional model captures only a rough average of the various sources of inhomogeneity. The second zone will contribute to the overall emission but will also partially absorb the light emitted from the first zone [59,60]. Following Ref. [13], the spectral radiance L_λ of a homogeneous, one-dimensional plasma is given by $L_\lambda = B_\lambda (1 - e^{-\tau_\lambda})$. Here B_λ is the Planck function, assuming local thermodynamic equilibrium (LTE) conditions. The subscript λ indicates the wavelength dependency of L_λ. In the exponent, τ_λ is the wavelength-specific optical depth [5,13]. The Planck function B_λ only depends on the wavelength and temperature and is independent of the ion density n_i [61]. The expected density and temperature values support our LTE approach (see, e.g., Ref. [5]) and small deviations from it do not meaningfully impact our qualitative analysis in the following. We now expand the model by adding a second layer of plasma. The first plasma layer emits the spectral radiance $L_{\lambda,1}$ over an optical depth $\tau_{\lambda,1}$. This light subsequently traverses a second plasma layer with an optical depth $\tau_{\lambda,2}$. The total spectral radiance $L_{\lambda,2}$ exiting the second layer of plasma is given by

$$L_{\lambda,2} = B_{\lambda,1} \left(1 - e^{-\tau_{\lambda,1}}\right) e^{-\tau_{\lambda,2}} + B_{\lambda,2} \left(1 - e^{-\tau_{\lambda,2}}\right), \tag{1}$$

where $B_{\lambda,1}$ and $B_{\lambda,2}$ are the respective blackbody functions of the two plasma layers. Next, we take two spectra obtained from plasma driven by 2-μm-laser light. These two spectra serve as base spectra for the model's two plasma layers [13]. Both spectra are, for simplicity, assumed to be generated from a single density-temperature plasma layer with significantly high optical depth ($L \approx B$ at peak emission wavelength) of value $\tau_{\lambda,i} \cdot a_i$ ($i = 1, 2$ for zones 1,2) with a constant multiplication factor a_i accounting for differences in density or length scales following the approach of Schupp et al. [13]. The optical depth of the plasma is expected to be reduced by a factor of up to 2 when going from 1- to 2-μm driver [43]. Given the large optical depth in the 1-μm case, as shown e.g. in Ref. [13], a sufficiently large optical depth is still to be expected in the current 2-μm case to remain within the limit of large optical depth at peak opacity (which is sufficient for our model).

In the following, the base spectrum of the first zone is associated with the maximum CE (cf. Fig. 4(c)). The base spectrum for the second zone is chosen from a modestly lower laser intensity, corresponding to a modestly lower plasma temperature conform our model. Following Ref. [5] the effective temperature of the first zone is set to 32 eV associated with optimum plasma conditions for producing in-band EUV light at the here expected plasma densities [5]. The plasma temperature of the second zone is subsequently found by matching the relative intensity values of the two base spectra at 13.5 nm wavelength (as $L \approx B$ at peak emission wavelength given the large optical depths involved [5,13] also for the 2-μm-driven base spectra). This results

in a temperature of 29 eV for the second zone. The model fit function $L_{\lambda,2}$ is then given by

$$L_{\lambda,2} = a_0 \left[B_{\lambda,1}(T = 32\text{eV})\left(1 - e^{-a_1 \tau_{\lambda,1}}\right) e^{-a_2 \tau_{\lambda,2}} + B_{\lambda,2}(T = 29\text{eV})\left(1 - e^{-a_2 \tau_{\lambda,2}}\right) \right]. \quad (2)$$

The multiplication factors a_i are used as free fit parameters, including an additional overall amplitude factor a_0. This amplitude factor a_0 is required because the measured 1-μm-driven spectrum cannot be normalized by the Planck function at peak emission wavelength, as in the case of the 2-μm-driven base spectra, since the observed self-absorption from a multi-(n_i, T) plasma voids the relation $L \approx B$ at peak emission wavelength. The a_0 fit value itself has no further physical meaning within the current context.

Fig. 5 shows the result of a least-squares fit of the model function Eq. 2 to the measured 1-μm-driven spectrum at a 2.5×10^{11} W/cm^2 laser intensity that reproduces the ionicity of the 2-μm-driven base spectrum (see Fig. 4(c)). The model is seen to excellently reproduce the data. The fit parameters obtained are $a_1 = 1.3$ and $a_2 = 0.7$, close to unity value such that the original base spectra are already representative of the emission of the two zones. A more quantitative interpretation of these fit values is not currently warranted given the qualitative nature of the model application. A comprehensive explanation of the generic effects of a two-zone plasma is provided in Ref. [59] albeit for hotter and denser plasma. EUV radiation, produced in the hottest part of the plasma, passes through regions of underheated plasma generated by the lower-intensity parts of the Gaussian laser intensity profile and the underheated plasma naturally present along the laser propagation, and rarefaction (z-)axis. The EUV emission in the case of the 1-μm-drive laser occurs at a higher plasma density than that of the 2-μm-driver and also its underheated plasma zone will have higher ion density. Hence, the 1-μm-LPP exhibits a higher EUV self-absorptivity (also see the work of Bouza et al. [62]) in the underheated zone making the 2-μm-LPP here the more efficient emitter of in-band EUV radiation. We note that self-absorption effects are absent in recent droplet-target experiments [43] in line with expectations given that the lower-intensity parts of the Gaussian-focus laser pulse do not interact with the small droplet target in that work.
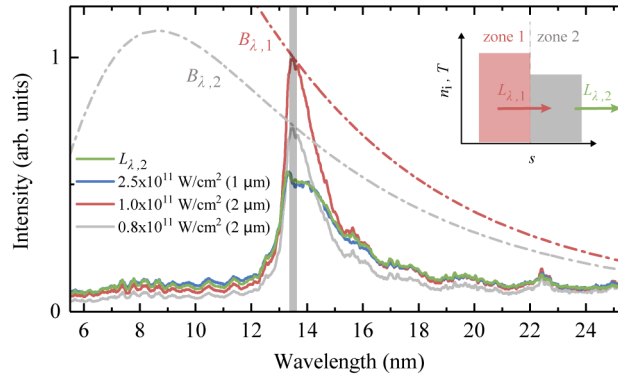
Fig. 5. Tin spectra from plasmas driven by 1- and 2-μm-lasers. The blackbody functions $B_{\lambda,1}$ and $B_{\lambda,2}$ are divided by $B_{13.5\text{ nm},1}$. The 2-μm-LPP spectra are scaled to be confined by their respective blackbody functions. The 1-μm-LPP spectrum is scaled according to the amplitude ratio of the respective spectra in Fig. 4(c). The green curve depicts the fit result of Eq. 1 to the 1-μm-LPP spectrum (see main text). The inset schematically depicts the model.

4. Conclusion

In conclusion, efficiencies of converting laser energy into in-band EUV photons into a 2π-sr half-sphere (CEs) in excess of 3% have been achieved from a Sn plasma driven by a 2-μm-wavelength laser system assuming isotropic emission. It here outperforms plasmas driven by a

1-μm-laser by a factor of two. The difference between the two drive laser cases can furthermore be qualitatively explained from self-absorption effects. Our findings regarding the scaling of the optimum laser intensity for efficient EUV generation and CE with drive laser wavelength are in broad agreement with the available literature, here moving into the territory between 1 and 10 μm wavelength. Further increases in CE are to be expected when providing a homogeneous heating of the plasma, optimizing the spatio-temporal intensity profile of the drive laser. Investigations of the EUV emission anisotropy enable to fully capture the emission characteristics. Such future studies, preferably executed on mass-limited droplet targets, will further pave the way for the application of 2-μm drive lasers in industrial sources of EUV radiation powering tomorrow's nanolithography.

References

1. O. O. Versolato, "Physics of laser-driven tin plasma sources of EUV radiation for nanolithography," Plasma Sources Sci. Technol. **28**(8), 083001 (2019).
2. M. Purvis, I. V. Fomenkov, A. A. Schafgans, M. Vargas, S. Rich, Y. Tao, S. I. Rokitski, M. Mulder, E. Buurman, M. Kats, J. Stewart, A. D. LaForge, C. Rajyaguru, G. Vaschenko, A. I. Ershov, R. J. Rafac, M. Abraham, D. C. Brandt, and D. J. Brown, "Industrialization of a robust EUV source for high-volume manufacturing and power scaling beyond 250W," in *Extreme Ultraviolet (EUV) Lithography IX*, vol. 10583 (SPIE, 2018), p. 1058327.
3. M. A. Purvis, A. Schafgans, D. J. W. Brown, I. Fomenkov, R. Rafac, J. Brown, Y. Tao, S. Rokitski, M. Abraham, M. Vargas, S. Rich, T. Taylor, D. Brandt, A. Pirati, A. Fisher, H. Scott, A. Koniges, D. Eder, S. Wilks, A. Link, and S. Langer, "Advancements in predictive plasma formation modeling," in *Extreme Ultraviolet (EUV) Lithography VII*, vol. 9776 (SPIE, 2016), pp. 159–170.
4. A. A. Schafgans, D. J. Brown, I. V. Fomenkov, R. Sandstrom, A. Ershov, G. Vaschenko, R. Rafac, M. Purvis, S. Rokitski, Y. Tao, D. J. Riggs, W. J. Dunstan, M. Graham, N. R. Farrar, D. C. Brandt, N. Böwering, A. Pirati, N. Harned, C. Wagner, H. Meiling, and R. Kool, "Performance optimization of MOPA pre-pulse LPP light source," in *Extreme Ultraviolet (EUV) Lithography VI*, vol. 9422 (SPIE, 2015), pp. 56–66.
5. F. Torretti, J. Sheil, R. Schupp, M. Basko, M. Bayraktar, R. Meijer, S. Witte, W. Ubachs, R. Hoekstra, O. Versolato, A. Neukirch, and J. Colgan, "Prominent radiative contributions from multiply-excited states in laser-produced tin plasma for nanolithography," Nat. Commun. **11**(1), 2334 (2020).
6. G. O'Sullivan, B. Li, R. D'Arcy, P. Dunne, P. Hayden, D. Kilbane, T. McCormack, H. Ohashi, F. O'Reilly, P. Sheridan, E. Sokell, C. Suzuki, and T. Higashiguchi, "Spectroscopy of highly charged ions and its relevance to EUV and soft x-ray source development," J. Phys. B **48**(14), 144025 (2015).
7. V. I. Azarov and Y. N. Joshi, "Analysis of the $4d^7$-$4d^6$ 5p transition array of the eighth spectrum of tin: Sn VIII," J. Phys. B **26**(20), 3495–3514 (1993).
8. S. S. Churilov and A. N. Ryabtsev, "Analysis of the spectra of In XII–XIV and Sn XIII–XV in the far-VUV region," Opt. Spectrosc. **101**(2), 169–178 (2006).
9. A. N. Ryabtsev, É. Y. Kononov, and S. S. Churilov, "Spectra of rubidium-like Pd X-Sn XIV ions," Opt. Spectrosc. **105**(6), 844–850 (2008).
10. H. Ohashi, S. Suda, H. Tanuma, S. Fujioka, H. Nishimura, A. Sasaki, and K. Nishihara, "EUV emission spectra in collisions of multiply charged Sn ions with He and Xe," J. Phys. B **43**(6), 065204 (2010).
11. J. Colgan, D. Kilcrease, J. Abdallah, M. Sherrill, C. Fontes, P. Hakel, and G. Armstrong, "Atomic structure considerations for the low-temperature opacity of Sn," High Energy Density Phys. **23**, 133–137 (2017).
12. F. Torretti, A. Windberger, A. Ryabtsev, S. Dobrodey, H. Bekker, W. Ubachs, R. Hoekstra, E. V. Kahl, J. C. Berengut, J. R. C. López-Urrutia, and O. O. Versolato, "Optical spectroscopy of complex open-4d-shell ions $Sn^7+ - Sn^{10}+$," Phys. Rev. A **95**(4), 042503 (2017).
13. R. Schupp, F. Torretti, R. A. Meijer, M. Bayraktar, J. Sheil, J. Scheers, D. Kurilovich, A. Bayerle, A. A. Schafgans, M. Purvis, K. S. E. Eikema, S. Witte, W. Ubachs, R. Hoekstra, and O. O. Versolato, "Radiation transport and scaling of optical depth in Nd:YAG laser-produced microdroplet-tin plasma," Appl. Phys. Lett. **115**(12), 124101 (2019).
14. R. Schupp, F. Torretti, R. Meijer, M. Bayraktar, J. Scheers, D. Kurilovich, A. Bayerle, K. Eikema, S. Witte, W. Ubachs, R. Hoekstra, and O. Versolato, "Efficient Generation of Extreme Ultraviolet Light From Nd:YAG-Driven Microdroplet-Tin Plasma," Phys. Rev. Appl. **12**(1), 014010 (2019).

15. J. Freeman, S. Harilal, B. Verhoff, A. Hassanein, and B. Rice, "Laser wavelength dependence on angular emission dynamics of Nd:YAG laser-produced Sn plasmas," Plasma Sources Sci. Technol. **21**(5), 055003 (2012).

16. S. Harilal, T. Sizyuk, A. Hassanein, D. Campos, P. Hough, and V. Sizyuk, "The effect of excitation wavelength on dynamics of laser-produced tin plasma," J. Appl. Phys. **109**(6), 063306 (2011).

17. S. Fujioka, H. Nishimura, K. Nishihara, A. Sasaki, T. Okuno, N. Ueda, T. Ando, Y. Tao, Y. Shimada, K. Hashimoto, M. Yamaura, K. Shigemori, M. Nakai, K. Nagai, T. Norimatsu, T. Nishikawa, N. Miyanaga, Y. Izawa, and K. Mima, "Opacity Effect on Extreme Ultraviolet Radiation from Laser-Produced Tin Plasmas," Phys. Rev. Lett. **95**(23), 235004 (2005).

18. H. Tanaka, A. Matsumoto, K. Akinaga, A. Takahashi, and T. Okada, "Comparative study on emission characteristics of extreme ultraviolet radiation from CO_2 and Nd:YAG laser-produced tin plasmas," Appl. Phys. Lett. **87**(4), 041503 (2005).

19. P. Hayden, A. Cummings, N. Murphy, G. O'Sullivan, P. Sheridan, J. White, and P. Dunne, "13.5 nm extreme ultraviolet emission from tin based laser produced plasma sources," J. Appl. Phys. **99**(9), 093302 (2006).

20. J. White, P. Dunne, P. Hayden, F. O'Reilly, and G. O'Sullivan, "Optimizing 13.5 nm laser-produced tin plasma emission as a function of laser wavelength," Appl. Phys. Lett. **90**(18), 181502 (2007).

21. C. W. Siders, A. C. Erlandson, T. C. Galvin, H. Frank, S. Langer, B. A. Reagan, H. Scott, E. F. Sistrunk, and T. M. Spinka, "Efficient high power laser drivers for next-generation High Power EUV sources," in *2019 Source Workshop*, (EUV Litho, Inc., 2019), pp. 1–23.

22. E. Sistrunk, D. A. Alessi, A. Bayramian, K. Chesnut, A. Erlandson, T. C. Galvin, D. Gibson, H. Nguyen, B. Reagan, K. Schaffers, C. W. Siders, T. Spinka, and C. Haefner, "Laser Technology Development for High Peak Power Lasers Achieving Kilowatt Average Power and Beyond," in *Short-pulse High-energy Lasers and Ultrafast Optical Technologies*, vol. 11034 (SPIE, 2019), pp. 1–8.

23. S. Langer, H. Scott, T. Galvin, E. Link, B. Regan, and C. W. Siders, "Simulations of Laser Driven EUV Sources - the Impact of Laser Wavelength," in *2020 Source Workshop*, (EUV Litho, Inc., 2020), pp. 1–25.

24. V. Bakshi, *EUV sources for lithography*, vol. 149 (SPIE press Bellingham, Washington, 2006), chap. 11.

25. M. Basko, "On the maximum conversion efficiency into the 13.5-nm extreme ultraviolet emission under a steady-state laser ablation of tin microspheres," Phys. Plasmas **23**(8), 083114 (2016).

26. K. Bergmann, S. V. Danylyuk, and L. Juschkin, "Optimization of a gas discharge plasma source for extreme ultraviolet interference lithography at a wavelength of 11 nm," J. Appl. Phys. **106**(7), 073309 (2009).

27. A. P. Shevelko, L. A. Shmaenok, S. S. Churilov, R. K. F. J. Bastiaensen, and F. Bijkerk, "Extreme Ultraviolet Spectroscopy of a Laser Plasma Source for Lithography," Phys. Scr. **57**(2), 276–282 (1998).

28. R. L. Kauffman, D. W. Phillion, and R. C. Spitzer, "X-ray production ~13 nm from laser-produced plasmas for projection x-ray lithography applications," Appl. Opt. **32**(34), 6897–6900 (1993).

29. S. S. Harilal, B. O. Shay, M. S. Tillack, Y. Tao, R. Paguio, A. Nikroo, and C. A. Back, "Spectral control of emissions from tin doped targets for extreme ultraviolet lithography," J. Appl. Phys. **39**(3), 484–487 (2006).

30. Y. Tao, S. Harilal, M. Tillack, K. Sequoia, B. O'Shay, and F. Najmabadi, "Effect of focal spot size on in-band 13.5 nm extreme ultraviolet emission from laser-produced Sn plasma," Opt. Lett. **31**(16), 2492–2494 (2006).

31. R. W. Coons, S. S. Harilal, D. Campos, and A. Hassanein, "Analysis of atomic and ion debris features of laser-produced Sn and Li plasmas," J. Appl. Phys. **108**(6), 063306 (2010).

32. R. C. Spitzer, T. J. Orzechowski, D. W. Phillion, R. L. Kauffman, and C. Cerjan, "Conversion efficiencies from laser-produced plasmas in the extreme ultraviolet regime," J. Appl. Phys. **79**(5), 2251–2258 (1996).

33. D. Campos, S. Harilal, and A. Hassanein, "The effect of laser wavelength on emission and particle dynamics of Sn plasma," J. Appl. Phys. **108**(11), 113305 (2010).

34. S. A. George, W. T. Silfvast, K. Takenoshita, R. T. Bernath, C.-S. Koay, G. Shimkaveg, and M. C. Richardson, "Comparative extreme ultraviolet emission measurements for lithium and tin laser plasmas," Opt. Lett. **32**(8), 997–999 (2007).

35. A. Z. Giovannini and R. S. Abhari, "Effects of the dynamics of droplet-based laser-produced plasma on angular extreme ultraviolet emission profile," Appl. Phys. Lett. **104**(19), 194104 (2014).

36. Y. Shimada, H. Nishimura, M. Nakai, K. Hashimoto, M. Yamaura, Y. Tao, K. Shigemori, T. Okuno, K. Nishihara, T. Kawamura, A. Sunahara, T. Nishikawa, A. Sasaki, K. Nagai, T. Norimatsu, S. Fujioka, S. Uchida, N. Miyanaga, Y. Izawa, and C. Yamanaka, "Characterization of extreme ultraviolet emission from laser-produced spherical tin plasma generated with multiple laser beams," Appl. Phys. Lett. **86**(5), 051501 (2005).

37. S. S. Harilal, R. W. Coons, P. Hough, and A. Hassanein, "Influence of spot size on extreme ultraviolet efficiency of laser-produced Sn plasmas," Appl. Phys. Lett. **95**(22), 221501 (2009).

38. Y. Ueno, G. Soumagne, A. Sumitani, A. Endo, and T. Higashiguchi, "Enhancement of extreme ultraviolet emission from a CO_2 laser-produced Sn plasma using a cavity target," Appl. Phys. Lett. **91**(23), 231501 (2007).

39. R. Amano, T.-H. Dinh, A. Sasanuma, G. Arai, H. Hara, Y. Fujii, T. Hatano, T. Ejima, W. Jiang, A. Sunahara, A. Takahashi, D. Nakamura, T. Okada, K. Sakaue, T. Miura, G. O'Sullivan, and T. Higashiguchi, "Influence of short pulse duration of carbon dioxide lasers on extreme ultraviolet emission from laser-produced plasmas," Jpn. J. Appl. Phys. **57**(7), 070311 (2018).

40. H. Mizoguchi, H. Nakarai, T. Abe, H. Tanaka, Y. Watanabe, T. Hori, Y. Shiraishi, T. Yanagida, G. Soumagne, T. Yamada, and T. Saitou, "Challenge of >300W high power LPP-EUV source with long collector mirror lifetime for semiconductor HVM," in *Extreme Ultraviolet (EUV) Lithography XI*, vol. 11323 (SPIE, 2020), pp. 225–238.

41. I. Fomenkov, D. Brandt, A. Ershov, A. Schafgans, Y. Tao, G. Vaschenko, S. Rokitski, M. Kats, M. Vargas, M. Purvis, R. Rafac, B. L. Fontaine, S. D. Dea, A. LaForge, J. Stewart, S. Chang, M. Graham, D. Riggs, T. Taylor, M. Abraham, and D. Brown, "Light sources for high-volume manufacturing EUV lithography: technology, performance, and power scaling," Adv. Opt. Techn. **6**(3-4), 173–186 (2017).

42. M. Yamaura, S. Uchida, A. Sunahara, Y. Shimada, H. Nishimura, S. Fujioka, T. Okuno, K. Hashimoto, K. Nagai, T. Norimatsu, K. Nishihara, N. Miyanga, Y. Izawa, and C. Yamanaka, "Characterization of extreme ultraviolet emission using the fourth harmonic of a Nd:YAG laser," Appl. Phys. Lett. **86**(18), 181107 (2005).

43. R. Schupp, L. Behnke, J. Sheil, Z. Bouza, M. Bayraktar, W. Ubachs, R. Hoekstra, and O. Versolato, "Characterization of 1- and 2-µm-wavelength laser-produced microdroplet-tin plasma for generating extreme-ultraviolet light," submitted for publication.

44. A. Kramida and Yu. Ralchenko J. R. and NIST ASD Team, NIST Atomic Spectra Database (ver. 5.3, 2015), http://physics.nist.gov/asd.

45. M. Bayraktar, H. M. Bastiaens, C. Bruineman, B. Vratzov, and F. Bijkerk, "Broadband transmission grating spectrometer for measuring the emission spectrum of EUV sources," NEVAC blad **54**, 14–19 (2016).

46. G. Arisholm, Ø. Nordseth, and G. Rustad, "Optical parametric master oscillator and power amplifier for efficient conversion of high-energy pulses with high beam quality," Opt. Express **12**(18), 4189–4197 (2004).

47. R. A. Meijer, A. S. Stodolna, K. S. E. Eikema, and S. Witte, "High-energy Nd:YAG laser system with arbitrary sub-nanosecond pulse shaping capability," Opt. Lett. **42**(14), 2758–2761 (2017).

48. S. S. Churilov and A. N. Ryabtsev, "Analyses of the Sn IX–Sn XII spectra in the EUV region," Phys. Scr. **73**(6), 614–619 (2006).

49. F. Torretti, R. Schupp, D. Kurilovich, A. Bayerle, J. Scheers, W. Ubachs, R. Hoekstra, and O. Versolato, "Short-wavelength out-of-band EUV emission from Sn laser-produced plasma," J. Phys. B **51**(4), 045005 (2018).

50. J. Scheers, C. Shah, A. Ryabtsev, H. Bekker, F. Torretti, J. Sheil, D. A. Czapski, J. C. Berengut, W. Ubachs, J. R. C. López-Urrutia, R. Hoekstra, and O. O. Versolato, "EUV spectroscopy of highly charged $Sn^{13+} - Sn^{15+}$ ions in an electron-beam ion trap," Phys. Rev. A **101**(6), 062511 (2020).

51. M. M. Basko, V. G. Novikov, and V. A. S. Grushin, "On the structure of quasi-stationary laser ablation fronts in strongly radiating plasmas," Phys. Plasmas **22**(5), 053111 (2015).

52. T. Sizyuk and A. Hassanein, "Tuning laser wavelength and pulse duration to improve the conversion efficiency and performance of EUV sources for nanolithography," Phys. Plasmas **27**(10), 103507 (2020).

53. T. Ando, S. Fujioka, H. Nishimura, N. Ueda, Y. Yasuda, K. Nagai, T. Norimatsu, M. Murakami, K. Nishihara, N. Miyanaga, Y. Izawa, K. Mima, and A. Sunahara, "Optimum laser pulse duration for efficient extreme ultraviolet light generation from laser-produced tin plasmas," Appl. Phys. Lett. **89**(15), 151501 (2006).

54. O. Morris, F. O'Reilly, P. Dunne, and P. Hayden, "Angular emission and self-absorption studies of a tin laser produced plasma extreme ultraviolet source between 10 and 18 nm," Appl. Phys. Lett. **92**(23), 231503 (2008).

55. K. L. Sequoia, Y. Tao, S. Yuspeh, R. Burdt, and M. S. Tillack, "Two dimensional expansion effects on angular distribution of 13.5nm in-band extreme ultraviolet emission from laser-produced Sn plasma," Appl. Phys. Lett. **92**(22), 221505 (2008).

56. C. Hong, L. Hui, C. Zi-Qi, L. Lu-Ning, T. Tao, Z. Du-Luo, L. Pei-Xiang, and W. Xin-Bing, "Experimental study on laser produced tin droplet plasma extreme ultraviolet light source," Acta. Phys. Sin. **64**, 075202 (2015).

57. C.-S. Koay, S. George, K. Takenoshita, R. Bernath, E. Fujiwara, M. Richardson, and V. Bakshi, "High conversion efficiency microscopic tin-doped droplet target laser-plasma source for EUVL," in *Emerging Lithographic Technologies IX*, vol. 5751 (SPIE, 2005), pp. 279–292.

58. S. Yuspeh, Y. Tao, R. Burdt, M. Tillack, Y. Ueno, and F. Najmabadi, "Dynamics of laser-produced Sn microplasma for a high-brightness extreme ultraviolet light source," Appl. Phys. Lett. **98**(20), 201501 (2011).

59. J. P. Apruzese, J. Davis, K. G. Whitney, J. W. Thornhill, P. C. Kepple, R. W. Clark, C. Deeney, C. A. Coverdale, and T. W. L. Sanford, "The physics of radiation transport in dense plasmas," Phys. Plasmas **9**(5), 2411–2419 (2002).

60. A. Sasaki, A. Sunahara, K. Nishihara, T. Nishikawa, K. Fujima, T. Kagawa, F. Koike, and H. Tanuma, "Atomic modeling of the plasma EUV sources," High Energy Density Phys. **3**(1-2), 250–255 (2007).

61. T. Krücken, K. Bergmann, L. Juschkin, and R. Lebert, "Fundamentals and limits for the EUV emission of pinch plasma sources for EUV lithography," J. Phys. D: Appl. Phys. **37**(23), 3213–3224 (2004).

62. Z. Bouza, J. Scheers, A. Ryabtsev, R. Schupp, L. Behnke, C. Shah, J. Sheil, M. Bayraktar, J. R. C. López-Urrutia, W. Ubachs, R. Hoekstra, and O. O. Versolato, "EUV spectroscopy of $Sn^{5+} - Sn^{10+}$ ions in an electron beam ion trap and laser-produced plasmas," J. Phys. B: At., Mol. Opt. Phys. **53**(19), 195001 (2020).